



Precise Calorimetry of Small Metal Samples Using Noise Thermometry

Jan Knapp^{1,2} · Lev V. Levitin¹ · Ján Nyéki¹ · Manuel Brando³ · John Saunders¹

Received: 20 June 2024 / Accepted: 21 August 2024
© The Author(s) 2024

Abstract

We describe a compact calorimeter that opens ultra-low-temperature heat capacity studies of small metal crystals in moderate magnetic fields. The performance is demonstrated on the canonical heavy fermion metal YbRh_2Si_2 . Thermometry is provided by a fast current sensing noise thermometer. This single thermometer enables us to cover a wide temperature range of interest from 175 μK to 90 mK with temperature-independent relative precision. Temperatures are tied to the international temperature scale with a single-point calibration. A superconducting solenoid surrounding the cell provides the sample field for tuning its properties and operates a superconducting heat switch. Both adiabatic and relaxation calorimetry techniques, as well as magnetic field sweeps, are employed. The design of the calorimeter results in an addendum heat capacity which is negligible for the study reported. The keys to sample and thermometer thermalisation are the lack of dissipation in the temperature measurement and the steps taken to reduce the parasitic heat leak into the cell to the tens of fW level.

Keywords Calorimetry · Ultra-low temperatures · Noise thermometry · Heavy fermion · Magneto-caloric effect

✉ Jan Knapp
jan.knapp@rhul.ac.uk
Lev V. Levitin
l.v.levitin@rhul.ac.uk
John Saunders
j.saunders@rhul.ac.uk

¹ Department of Physics, Royal Holloway University of London, Egham Hill, Egham TW20 0EX, UK

² Department of Physics, University of Oxford, Parks Road, Oxford OX1 3PU, UK

³ Physics of Quantum Materials, Max Planck Institute for Chemical Physics of Solids, Nöthnitzer Straße 40, Dresden 01187, Germany

1 Introduction and Overview

Measurements of thermodynamic quantities are key to understanding order and excitations in quantum materials. For the measurement of heat capacity by the adiabatic method, the sample needs to be thermally separated from its environment, which poses technical challenges. Numerous designs of calorimeters have been developed for the temperature range 0.01–1 K, dealing with adiabatic isolation in a variety of ways [1–6], and references therein. Surprisingly, ultra-low temperatures can simplify this issue because heat capacities and conductivities of structural materials can become vanishingly small. However, complications in the choice of thermometry and the need to limit parasitic heat leaks into the experimental setup make heat capacity studies below 1 mK relatively scarce. Heat capacity measurements performed at ultra-low temperatures by the group in Bayreuth helped to resolve the interplay of (nuclear) magnetism and superconductivity in materials such as pure aluminium [7] and indium [8] as well as the AuIn₂ alloy [7, 9]. They achieved extremely low temperatures, often using the sample itself as the refrigerant. However, such samples can be relatively large.

By contrast, quantum materials such as heavy fermion metals are often only available in the form of small single crystals. Our calorimeter demonstrated outstanding performance with a state of the art 22 mg single-crystal sample of YbRh₂Si₂ [10, 11]; however, we argue that its simple design can be used for a wide range of materials. Using pure and well-characterised construction materials, with state-of-the-art thermometry and shielding, we succeeded in measuring the heat capacity with unprecedented precision and accuracy over the temperature range 175 μ K–90 mK [12]. The calorimeter is currently installed on a copper nuclear demagnetisation stage precooled by a wet dilution refrigerator.

The design of the calorimeter is illustrated in Fig. 1, as a combination of a microscope photograph and a schematic of the wiring. All essential components in the cell are made and connected with the sample by small pieces of wire much smaller than the sample itself. This was done by using well-established techniques of spot-welding and ultrasonic wire bonding. Such a compact design ensures the addendum heat capacity, which is the heat capacity of everything inside the cell apart from the sample, is negligible, as demonstrated in Fig. 2. This typical addendum serves as a reference for the selection of potential quantum material samples that might be studied with our technique.

Current sensing noise thermometry (CSNT) [14–17] was used over the full temperature range. Here, it was implemented as a local probe on a small sample for calorimetry for the first time, with the sensor resistance selected for fast measurement time. The requirements are more stringent than in our recent use of noise thermometry to measure the heat capacity of a PrNi₅ nuclear demagnetisation stage [18]. The noise thermometer and a heater are both made out of Pt₉₂W₈ (for simplicity PtW) ribbon, an alloy with negligible temperature dependence of resistivity, low magneto-resistance, and small heat capacity [19, 20]. The ribbon was produced by flattening \varnothing 50 μ m PtW wire. The noise thermometer is located on the opposite side of the sample to the heater and an aluminium heat switch,

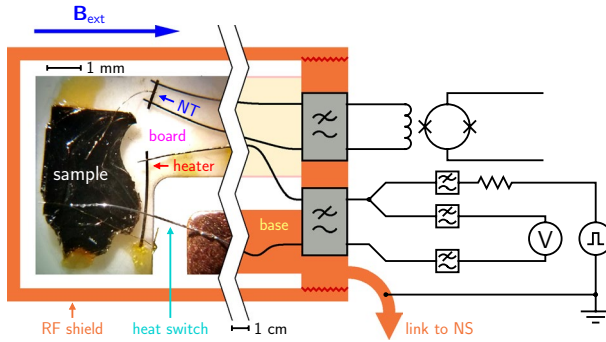


Fig. 1 Design of the calorimetry cell. The key interior components are illustrated with a photograph, the rest of the setup is shown schematically. A sample (here a single crystal of YbRh_2Si_2) is thermalised to the copper base of the cell via an ultrasonically bonded aluminium heat switch. The copper base is cooled by the nuclear stage (NS) of an adiabatic demagnetisation refrigerator. Heater and noise thermometer (NT), made out of PtW ribbons, are connected to the sample via spot-welded gold wires, the electrical connections are made with spot-welded niobium wires. The sample, heater, and NT are glued to an alumina (sintered Al_2O_3) board with GE varnish. The cell is radio-frequency (RF) tight with silver epoxy low-pass filters interrupting all electrical lines. The heater is driven by a pulse generator via a cold ballast resistor, with the heat switch and cryostat ground forming part of the current path. Additional electrical connections enable in situ measurement of the heater resistance. The cell is situated inside a compact superconducting solenoid, that provides the sample field B_{ext} and controls the heat switch

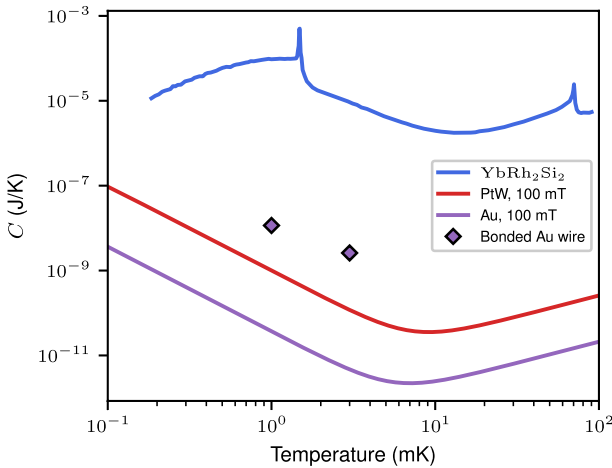


Fig. 2 Measured heat capacity of YbRh_2Si_2 vs. an estimate of the addendum heat capacity of the empty cell from the known amount of Au (6 mm of $\phi 25 \mu\text{m}$) and PtW (3.5 mm of $\phi 50 \mu\text{m}$) wires used, demonstrating that the addendum is negligible. The lines consist of a linear in T electronic and a Schottky T^{-2} nuclear heat capacity. Purple diamonds represent the heat capacity of a similar Au wire bonded to Au pads evaporated on silicon measured in zero magnetic field [13]. This relatively large value is attributed to the nuclear quadrupolar moments in crystallographically imperfect gold. All other structural materials of the cell either have a vanishingly small heat capacity, or the heat capacity is separated by a large enough thermal resistance, e.g. the nuclear heat capacity of aluminium inside Al_2O_3

helping to ensure that it accurately captures the temperature of the sample. In the following, we describe the essential components in more detail and report on their performance.

2 Heat Switch

To approach nearly perfect adiabatic isolation, the sample rests on a board made out of a good insulator, sintered Al_2O_3 (alumina). The 0.5-mm-thick board is fixed to the copper or silver base and extends 18 mm into free space. The base is well thermalised to our microkelvin cryostat via a cone joint. The sample is precooled via a superconducting heat switch. We have successfully used aluminium and lead.

2.1 Aluminium Heat Switch

The sample is connected to the copper base by an ultrasonically bonded $\varnothing 50\ \mu\text{m}$ aluminium wire. The heat switch operates at the critical field of aluminium $\mu_0 H_c = 10\ \text{mT}$ and enables measurements of heat capacity by adiabatic methods, described in Sects. 5 and 7, in fields up to H_c . At higher fields, the heat capacity can be measured by the relaxation method (see Sect. 6), albeit over a limited temperature range. Figure 3 illustrates the regimes of temperature and magnetic field, where different methods apply to the combination of our YbRh_2Si_2 sample, aluminium heat switch, and fast noise thermometer with typical sampling period of 50 s.

The normal state electrical resistance of the aluminium heat switch was measured to be $1.5\ \text{m}\Omega$ at 4 K, dominated by the wire bond of Al to YbRh_2Si_2 , as the resistance of the wire itself is estimated to be $0.2\ \text{m}\Omega$. In comparison, the state-of-the-art Cu-Au-Al-Au-Cu heat switches achieve $\text{n}\Omega$ level [21]. This imperfection, that we attribute to oxidation or general unfitness of the wire bonding to the combination of Al

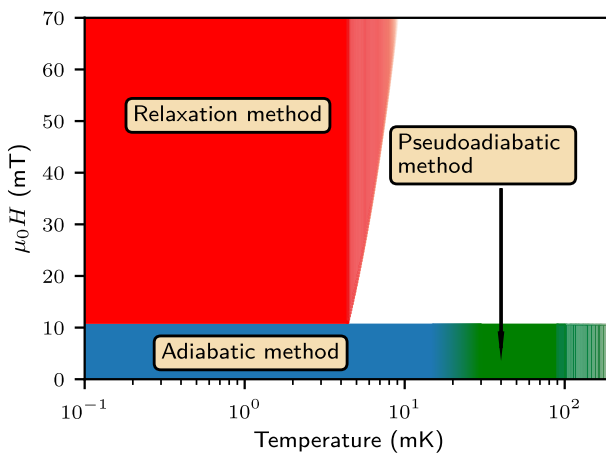


Fig. 3 Temperature—applied magnetic field map of the pulsed calorimetry methods used with the aluminium heat switch

and YbRh_2Si_2 , was favourable to our measurements: The heat switch simultaneously provided fast precooling of the sample (e.g. in 12 mT, the sample cooled from 10 to 0.4 mK in 6 h) and allowed relaxation measurements over a relatively broad temperature range. The normal state thermal conductivity of the heat switch, inferred from the time constants of thermal relaxation (e.g. Fig. 9) and measured heat capacity, is consistent with Wiedemann–Franz law for the $\text{m}\Omega$ electrical resistance.

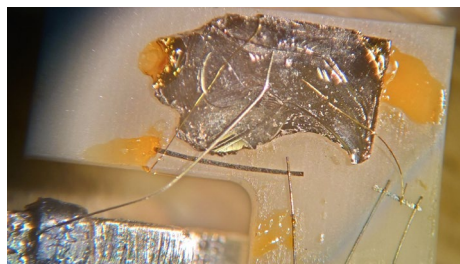
The combination of the alumina board and aluminium heat switch in the superconducting state results in excellent adiabatic isolation. Below 10 mK, an upper bound on the parasitic thermal conductance of 100 fW/K was inferred from the undetectable change in the measured heat leak to the isolated sample sitting at a few hundred μK , when the nuclear stage temperature is deliberately raised from 1 to 10 mK. By 90 mK, this thermal conductance increases by four orders of magnitude, leading to pseudo-adiabatic heat capacity measurements, see Sect. 5. No heat release was detected when opening the heat switch, enabling adiabatic heat capacity measurements below 200 μK .

2.2 Lead Heat Switch

In order to extend the magnetic field range over which adiabatic methods can be employed, a second generation cell was constructed with a lead heat switch. Lead is also a type I superconductor with a larger critical field $\mu_0 H_c = 80 \text{ mT}$. However, due to softness of lead, it is difficult to obtain fine wires or use ultrasonic bonding. The sample was moved from the copper base, shown in Fig. 1, to an identical base made out of pure silver, Fig. 4. Lead is relatively easy to join with silver because the phase diagram of their mixtures features an eutectic point at 304°C and 95.5% atomic percentage of lead [22]. The eutectic character of the emerging Pb–Ag alloy ensures a clear transition from the superconductor to highly conducting normal metal across the joint. We created a “bead” of pure lead on the silver cell base by melting it with a clean soldering iron on the surface of the base. A $\varnothing 50 \mu\text{m}$ pure silver wire was spot-welded to the YbRh_2Si_2 sample and to the lead, making the construction of the heat switch relatively easy.

The normal state resistance of the lead switch is less than 1 $\text{m}\Omega$ and was not determined precisely. The associated thermal conductance is higher than that of the aluminium switch, resulting in fast precools into the μK regime. These may have been further facilitated by the reduced nuclear magnetic heat capacity of the silver

Fig. 4 The calorimetry cell with the lead heat switch. The lead “bead” is visible in the bottom left corner, with the interconnecting silver wire spot-welded to the “bead” and the sample



base in comparison with copper [1]. All measurements with the lead heat switch were taken with the switch open, in superconducting state.

The ratio of normal and superconducting thermal conductivity, the switching ratio, depends on the Debye temperature θ of the material to the second power [1]. Aluminium is, therefore, a highly favourable material for the construction of heat switches, because $\theta_{\text{Al}} = 428$ K, while $\theta_{\text{Pb}} = 105$ K, making the expected switching ratio of an identical lead heat switch approximately 8 times smaller than aluminium. We note that this is despite the much greater critical temperature of lead compared to aluminium. The lead switch leaked visibly at temperatures as low as 4 mK, and the measurement method evolved from (pseudo-)adiabatic to relaxation across 4–90 mK range.

Unlike aluminium, the opening of the lead heat switch at the lowest temperature was always associated with a heat release, of the order of 10 nJ. Consequently, the starting temperature of the measurements was typically 500 μK , even though the sample had been cooled down to 300 μK prior to opening the heat switch. This heat release is much greater than the expected latent heat of the normal to superconducting transition of a type I superconductor $L(T) = -2\mu_0 H_c^2(T=0)(T/T_c)^2 [1 - (T/T_c)^2] V$, where H_c , T_c , and V are the critical field, critical temperature, and volume of the superconductor, respectively [23]. The latent heat calculated for the construction of our lead heat switch is in the fJ range, indicating some other source of heat release, such as the dissipation when magnetic flux is expelled from the sample, since the lead bead has a rather bulky and irregular shape compared to the aluminium wire.

3 Noise Thermometer

Our calorimeter is distinguished by the use of current sensing noise thermometry (CSNT). The CSNT can be made exceptionally small, since the sensor itself is just a snippet of normal conductor. In our case, a section of PtW ribbon with a relatively large resistance $R = 203$ m Ω was selected. This results in a large bandwidth over which the noise is measured, enabling fast temperature acquisition [14–17]. This noise thermometer typically measures with a 1% relative precision in about 50 s, independent of temperature, with the relative precision scaling as inverse square root of measuring time.

The thermal conductivity of the ribbon can be estimated using the Wiedemann–Franz law. Such a large sensor resistance severely limits the parasitic heat leak to the thermometer that can be tolerated, to around 2 fW in order to ensure thermal equilibrium within 10% at 200 μK . This is achievable with appropriate filtering [13]. The CSNT method is essentially non-dissipative, requiring no external excitation. A white noise voltage arises from thermal agitation of charge carriers [24, 25]. The sample is connected to the input coil of a superconducting quantum interference device (SQUID) via a superconducting flux transformer. A two-stage SQUID sensor [26, 27] is used, operating as a sensitive current amplifier. It is located remotely from the calorimeter, mounted on the still plate of the dilution refrigerator. This technique is in principle a primary thermometer [15, 28], capable of yielding true thermodynamic temperature if all electrical parameters are known. More conveniently, the

thermometer can be calibrated with high accuracy at a single temperature, since the temperature dependence of the noise voltage derives from a fundamental physical law. It is advantageous that the calibration point can be chosen at any temperature in the range of operation of the noise thermometer. On our cryostat, a calibrated germanium resistance thermometer, compared to a ^3He melting curve thermometer, was used to provide the calibration point for the cell CSNT at 200 mK, where the calorimetry cell was in thermal equilibrium with both the nuclear stage and the mixing chamber. This ties the measurement to the international temperature scale [28–30].

For measurements of heat capacity, fast temperature readings are essential. This is achieved by measuring the current fluctuations over a large bandwidth. The bandwidth R/L_i of a CSNT is given by the resistance R of the sensor and the SQUID input coil inductance $L_i = 1.6\mu\text{H}$, emphasising the need for a high resistance sensor. The thermometer bandwidth is typically still smaller than the full acquisition bandwidth capability of the SQUID amplifier. In our case, 2^{17} points are recorded with 1 MHz sampling frequency using a digital oscilloscope from National Instruments [31]. The recorded signal is Fourier transformed, and the power spectral density averaged 200 times. The flux noise power spectrum is

$$S_\Phi = 4k_B\text{TR} \frac{M_i^2}{R^2 + L_i^2\omega^2} + S_\Phi^0, \quad (1)$$

where $M_i = 7.1$ nH is the mutual inductance of the input coil and the first stage of the SQUID sensor, and S_Φ^0 is the noise contribution to the measurement from the SQUID itself, which we consider to be white. The comparison of the white noise produced by the sensor and the SQUID determines the noise temperature of the setup, which is 13 μK in our case, well below the lowest temperature ever measured.

Figure 5 shows examples of current sensing noise thermometer spectra taken at 198 μK and 201 mK in zero magnetic field, accompanied by a spectrum taken at 336 μK in 70 mT. Whereas the 201 mK spectrum is almost completely free from spurious noise and can be fitted by Eq. 1 after removing a single peak at 4 kHz, the spectra at ultra-low temperature, and especially in a magnetic field, are polluted by vibrational noise peaks to a much greater extent. These peaks are easily removed by an iterative discrimination procedure and do not significantly influence the measurement accuracy [14]. At the lowest temperatures, the white noise S_Φ^0 and a $1/f$ noise contributions of the SQUID become more significant. The SQUID white noise is determined from the highest frequency part of the spectrum. It is left as free parameter in the fits, since it can vary with the temperature of the SQUID itself, which is about 0.6 K, the temperature of the still plate of our dilution refrigerator. The $1/f$ noise has less influence in a large bandwidth noise thermometer, as the part of the spectrum below 1 kHz is simply not used, as shown in Fig. 5. The maximum estimated uncertainty in T after accounting for these last two contributions occurs at the lowest temperature and is less than 5%.

The resistive element of a CSNT can be made out of any normal metal, but the PtW alloy is advantageous in terms of resistivity and its negligible temperature dependence, low magnetoresistance, small heat capacity [19, 20], and general

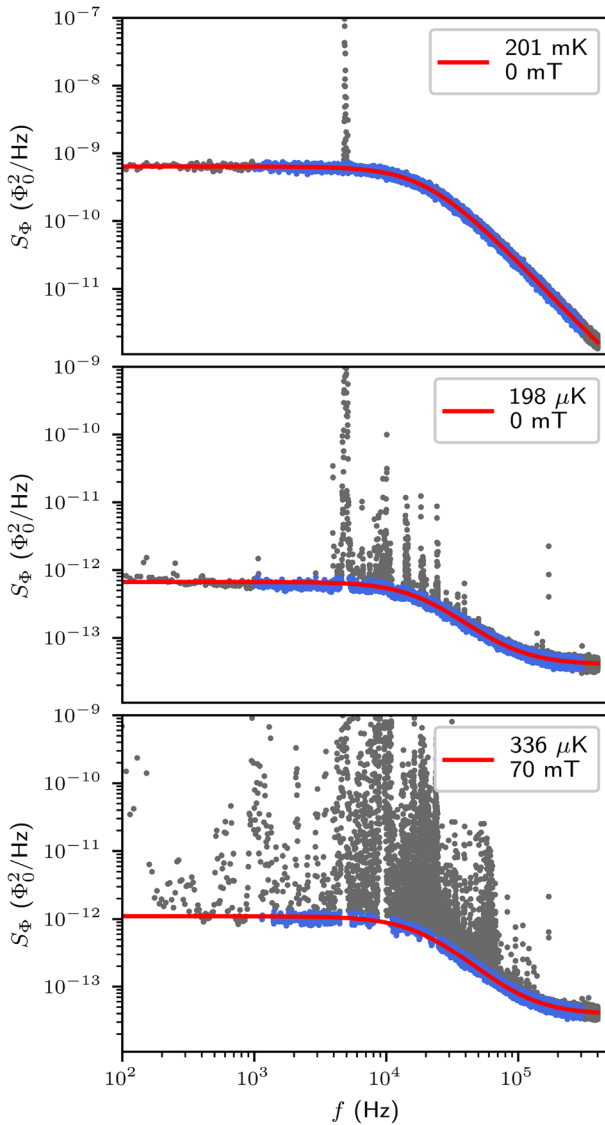


Fig. 5 Noise thermometer spectra taken at three different temperatures and two applied fields. Points from the frequency range 1–300 kHz (blue) are fitted with Eq. 1, with T and S_{Φ}^0 as the fitting parameters. Grey points were discarded by an iterative discrimination procedure [14]. In addition to the fitted terms, the $1/f$ contribution to the SQUID noise is apparent at low temperatures and frequencies

metallurgical properties. The PtW ribbon is spot-welded at both ends to $\varnothing 50 \mu\text{m}$ Nb wires that act as thermal breaks. The phase diagram of Pt and Nb features a rich number of alloys with very high melting points [32]; we find that their spot-welds tend to be very stable and reliable both mechanically and resistively. The noise thermometer is thermalised to the sample by a gold $\varnothing 25 \mu\text{m}$ wire, which is

spot-welded to the middle of the PtW ribbon, and on the other end to the sample. These spot-welds were also observed to be very reliable, despite a low solubility of Au and Pt [33]. Most importantly, they are not highly resistive, or superconducting, and do not deteriorate with time.

4 Heater

The ohmic heater with 0.9Ω resistance is also made out of the PtW ribbon. The current enters via a spot-welded Nb wire serving as the I_+ lead. On the other end of the ribbon, a spot-welded gold wire interconnects the heater with the sample. The current flows through the relatively bulky sample, of negligible resistance, and into the cold cryostat ground (I_-) via the heat switch. The heating pulse is produced by a voltage or current source at room temperature, connected between the I_+ current lead and the room temperature body of the cryostat, with a cold $100 \text{ k}\Omega$ ballast resistor located on the current line at 0.6 K protecting the cell from thermoelectric and other parasitic voltage sources. Additional electrical connections to the heater enable in situ measurement of the heater resistance.

Figure 1 shows that the cell is located inside of a continuous metal enclosure, formed by the copper body of the experimental platform and a silver epoxy filter and seal, developed originally to cool down two-dimensional electron gas to ultra-low temperatures [13]. The noise thermometer and heater (I_+/V_+ and V_-) leads were individually twisted and fully submerged into the silver epoxy [34] over a length of 82 cm . In our 4 K tests, such silver epoxy low-pass filters were found to have a cut-off frequency of about 100 MHz . The heater wiring has an additional low-pass filter installed at the mixing chamber. Inside the rf-shielded box of the filter, the I_+ and V_+ coaxial cables from room temperature were connected to the single ongoing I_+/V_+ lead, entering the cell. Together with the V_- lead, these three lines were each interrupted by $1 \text{ k}\Omega + 10 \text{ nF}$ T-filters. These filters, with approximately 15 kHz cut-off frequency, further protected the heater from external interference.

To apply heat, we used an arbitrary waveform generator from National Instruments [35] or a Keithley 2400 SMU [36]. The former is most suited for producing short pulses, while the latter for producing constant heating current. Extracting the heat capacity from heater pulses is the most common calorimetry method and can be done in the state of adiabatic isolation, as well as in the relaxation regime; an example of the pulse measurement in the former regime, at the lowest achieved temperature of $175 \mu\text{K}$, is shown in Fig. 6, while typical relaxation from pulses, done in 60 mT , is shown in Fig. 9. The continuous warm-up method, demonstrated in Fig. 10, is a useful complement to the standard pulse method, especially in the vicinity of phase transitions. Finally, magneto-caloric sweeps, which are done without use of the heater, are introduced as another useful tool for characterising phase transitions and magnetic phases in Fig. 11. In subsequent sections, we describe the results of these methods in more detail.

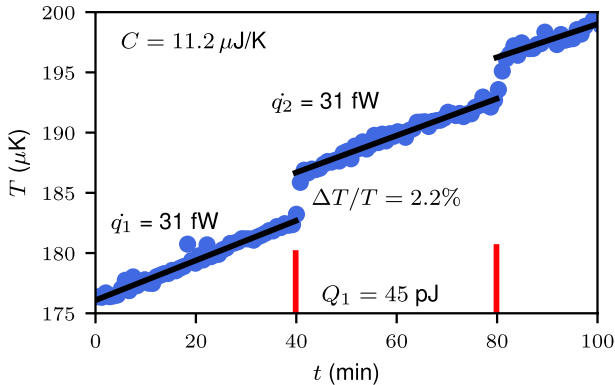


Fig. 6 Typical heat pulses and temperature drifts at the lowest achieved temperature of 175 μK . Pulses (in red) of the order of 45 pJ were applied every 40 min, resulting in units of percent increase in temperature, while the drifts in between them accurately determine the parasitic heat leak \dot{q}_i

5 Adiabatic Pulse Method

Applying a pulse of energy Q and observing the temperature increase $\Delta T = T_h - T_l$ from T_l to T_h as a result of the pulse, the heat capacity of the sample at mean temperature $T = (T_h + T_l)/2$ is

$$C = \frac{Q}{\Delta T}. \quad (2)$$

The size of the pulse $\Delta T/T$ must be optimised based on technical performance of the cell. As shown in Fig. 6, the temperature drifts in-between pulses result from the parasitic heating \dot{q} to the sample. The longer the temperature drift is observed for, the more precise is the determination of T_l and T_h . The uncertainty in $T_{l,h}$ scales with the number of temperature readings in the drift N as $1/\sqrt{N}$. However, recording the drifts for a long time is not advantageous if the heat capacity is strongly temperature dependent, as in the vicinity of a phase transition. Thus, it is essential to achieve a small parasitic heat leak into the calorimeter and a sufficiently high precision of the temperature, determined in a suitable measurement time (constrained by the temperature drift rate). Here, these challenges are met by the large bandwidth noise thermometer, which achieves a 1% precision in only 50 s, and the state-of-the-art shielding of the cell, and filtering of the incoming leads, which reduces the parasitic heat leak to 30 fW, inferred from linear fits to the temperature drifts between individual pulses and the heat capacity determined from the pulses (see Fig. 6.)

We believe that this heat leak is mostly deposited into the sample, since in a similar environment, the heat leak to the noise thermometer alone was found to be 0.1 fW [13]. Thanks to these technical achievements, it is possible to probe the sample with very small pulses, typically of the order of $\Delta T/T \approx 1\%$, but also much less ($\Delta T/T \approx 0.1\%$) where the heat capacity is large. This allowed precise investigation of the low-temperature phase transition T_A in YbRh_2Si_2 [12, 37–39] in the present application.

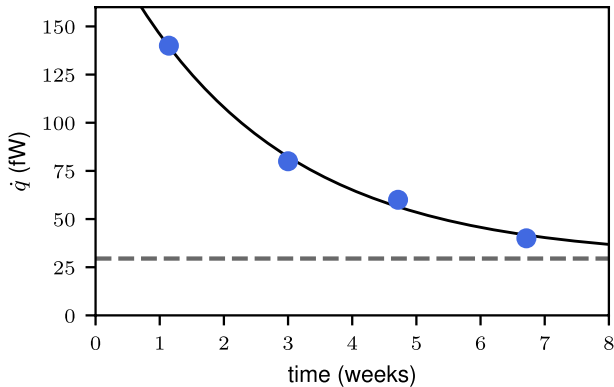


Fig. 7 Time dependence of the heat leak into the YbRh_2Si_2 calorimetry cell after the initial cool down of the cryostat. The measurements were performed in zero magnetic field at temperatures around 1 mK. This measurement reveals an intrinsic time-dependent heat release, vanishing exponentially, and a residual heat leak of about 30 fW

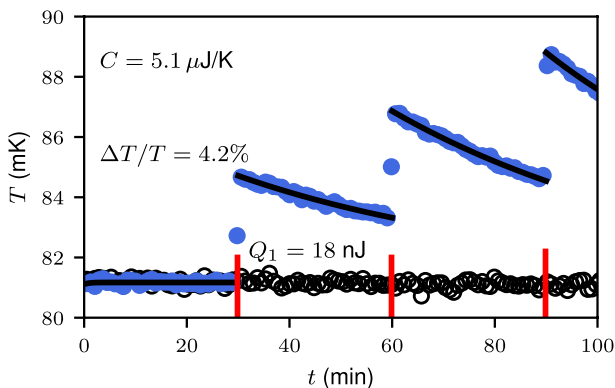


Fig. 8 Typical heat pulses and temperature drifts towards the upper end of the temperature range of the adiabatic method where the heat switch or alumina board starts to leak. In this example, the sample magnet is in 0 mT, and the temperature of the cryostat (black circles) is stabilised

The parasitic heat leak is found to decay over time following the cool down of the cryostat from room temperature, Fig. 7. We attribute this to heat release of unknown origin in the sample itself or nearby components. Nonetheless, the residual parasitic heat leak observed after about 8 weeks following the initial cooldown is very low. Without application of external heat, the small sample would remain below 1 mK for 20 days, when initially cooled down to the lowest temperature of 175 μK , and it would take it additional 23 days to warm up above the T_A transition.

The adiabatic technique was also shown to work well at typical dilution refrigerator temperatures. An example at 80 mK is shown in Fig. 8. The relaxation after the pulse arises from the thermal conductivity of the superconducting heat switch and

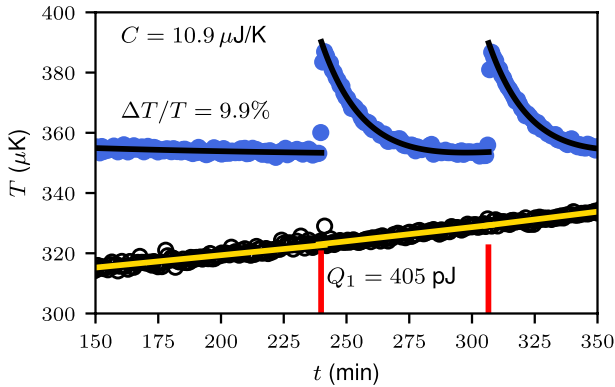


Fig. 9 Example of the relaxation method in 60 mT. The sample temperature (blue circles) shows relaxation from pulses, while the cryostat (black circles) is warming at the background. The cryostat's drifts between pulses are approximated by yellow lines. Internal time constants of the sample appear to be very small, the sample temperature rises to the full amplitude within two temperature readings, i.e. 100 s. The relaxation after the pulse is fitted by a sum of exponential and linear functions, where the linear part uses the cryostat's drift as a guidance

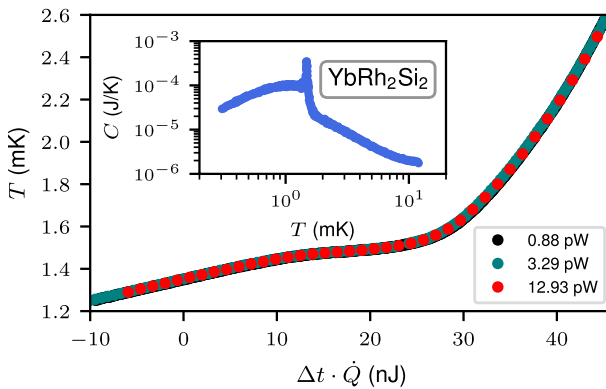
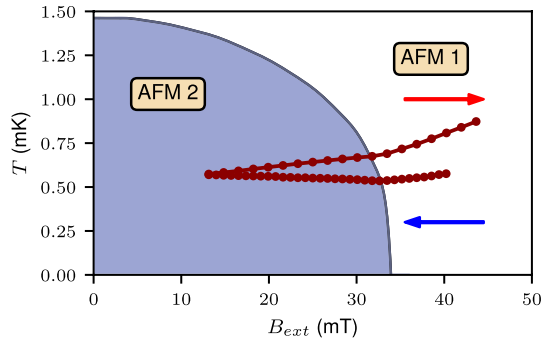


Fig. 10 Continuous warm-up across the T_A low-temperature phase transition in YbRh_2Si_2 under three different heat loads. The warm-up curves can be collapsed, scaling the time axis by the total heat load \dot{Q} (quoted in the legend), the sum of applied power and the heat leak of 0.08 pW. The inset shows heat capacity obtained from the warm-up in $\dot{Q} = 3.29$ pW, which manifests the peak at T_A in its sharpness and accurately agrees with the pulse method results, shown in Fig. 2

the alumina board, so we refer to this method as pseudo-adiabatic. Such measurements were possible up to 10 mT for the aluminium switch and up to 65 mT for the lead switch above which it leaked significantly.

Fig. 11 Magneto-caloric sweeps in YbRh_2Si_2 . Blue- and red-coloured arrows indicate the direction of the sweeps as demagnetisation and magnetisation, respectively. The vertical difference between the sweep up and down is proportional to the parasitic heat deposited in the sample during the sweep. The phase transition is clearly marked by a change of slope



6 Relaxation Method

The relaxation method was used in fields above 10 mT, when the aluminium heat switch was in the normal state, and at high temperatures, where the lead heat switch leaked significantly even in the open state. The heat capacity is again inferred from Eq. (2), with the temperature T_h obtained by extrapolating the observed relaxation back to the moment of the heat pulse, see Fig. 9. To use this method, the temperature measurement time must be much shorter than the time constant $\tau \approx C/k$ of the thermal relaxation of the sample temperature, where C is the sample heat capacity, and k is the thermal conductance to the cryostat (dominated by the heat switch).

Following a small pulse, thermal relaxation of the sample to the bath of constant temperature is typically exponential. Taking into account a slow underlying temperature drift of the cryostat temperature, the relaxation was fitted to $T(t) = a \exp(-t/\tau) + bt + c$. This equation was used to extrapolate temperature both before and after the pulse, yielding T_l and T_h for Eq. (2).

Furthermore, for the relaxation method to work, the thermal diffusivity across the sample and the coupling between various degrees of freedom of the sample must be strong, such that the associated time constants of the internal sample thermalisation are also short in comparison with τ . In metals, the coupling of electrons and nuclei is given by the Korringa constant $\kappa = \tau_1 T_e$, where τ_1 is the nuclear spin–lattice relaxation time and T_e the electronic temperature. In metals with a strong hyperfine coupling of nuclei and electrons, as is the case of YbRh_2Si_2 [40–47], the Korringa constant is expected to be short, as established in PrNi_5 [1]. The immediate transfer of heat to the nuclear system apparent in Figs. 6 and 9 supports this expectation of “fast coupling”.

With the aluminium heat switch, it was possible to measure the heat capacity of YbRh_2Si_2 using the relaxation method, in fields above 10 mT, up to about 4 mK. In this case, the limitations were the conductance of the heat switch increasing linearly with temperature, while the heat capacity of predominantly nuclear origin decreasing approximately as $T^{-1.5}$ in this temperature range. This causes the thermal time constant τ to quickly become comparable to the noise thermometer acquisition time, which is where the method fails. Clearly, the combination of sample and thermal link can be optimised to extend the temperature range where the relaxation method

can be employed, but this was beyond the scope of the present work. As discussed earlier, extending the temperature range of measurements in fields greater than 10 mT was achieved by implementing the lead heat switch.

7 Continuous Warm-Up Method

The continuous warm-up method is extremely useful when studying anomalies and phase transitions. When the sample is firmly in the adiabatic regime, the heat capacity is extracted from a warm-up record $T(t)$ under the steady heat load \dot{Q} as

$$C = \frac{\dot{Q}}{\partial T / \partial t}. \quad (3)$$

Here \dot{Q} is the sum of the power applied to the heater and the parasitic heat leak. The density of thus obtained $C(T)$ points increases with decreasing \dot{Q} , and at very low \dot{Q} , the adjacent $T(t)$ points may need to be averaged to reduce the scatter in $\partial T / \partial t$.

Here, we probed the low temperature T_A transition in YbRh_2Si_2 in zero field, as shown in Fig. 10. Warm-ups were recorded under three different steady powers, and the heat leak of 80 fW was found to collapse the datasets. The heat capacity inferred according to Eq. (3) is in perfect agreement with that obtained using heat pulses. From the continuous warm-ups, we infer that the T_A transition is second order: There is no signature of a plateau in the warm-up curve in Fig. 10 that would indicate a latent heat.

8 Field Sweeps

In this section, we describe the use of field sweeps in the detection of a field-induced phase transition in YbRh_2Si_2 , exploiting the magneto-caloric effect. In this context, YbRh_2Si_2 is an example of a hyperfine enhanced nuclear refrigerant; its 4f electronic moment grows with the applied magnetic field, resulting in a much stronger field on the Yb nucleus, due the hyperfine interaction [12, 48, 49]. Our measurements of the moment growth (in the ab-crystallographic plane), combined with the hyperfine constant of Yb, $102 \text{ T}/\mu_B$ [40–42], determine the amplification ratio of the field applied to that felt by the nucleus to be about 150. A magneto-caloric field sweep of YbRh_2Si_2 is shown in Fig. 11. A clear feature in the field-induced temperature sweep is observed, marking a phase transition. We observe the magneto-caloric effect to be stronger in the primary antiferromagnetic order in YbRh_2Si_2 [12, 50, 51], observed above about 35 mT as $T \rightarrow 0$. However, even in the low field phase, which we identified to be a form of a spatially modulated magnetic order [12], the temperature can be lowered by demagnetisation, as was observed by a faster field sweep. This technique has thus proved valuable to map the phase boundary near a quantum phase transition driven by magnetic field, where the critical temperature decreases strongly with field.

9 Conclusions

The design of the heat capacity cell described in this paper has the advantages of simplicity and modularity, which make it suitable for a large variety of quantum materials. When adapting it for a particular metal sample, the outstanding question is always the common metallurgy of the sample and interconnecting wires and the addendum heat capacity, which determines which materials and bonding techniques to use. The recent advances in fast current sensing noise thermometry [14–17] make this an attractive choice for calorimetry at dilution refrigerator temperatures and below. Together with the filtering and shielding of superconducting leads, we have implemented it brings calorimetry and bolometry (see review [52]) to an improved level of sensitivity, in terms of sample size, and should have far-reaching consequences for future fundamental research.

Acknowledgements This work was supported by European Union's Horizon 2020 Research and Innovation programme under Grant Agreement No. 824109 (European Microkelvin Platform) and the Deutsche Forschungsgemeinschaft (DFG, German Research Foundation) through Grants No. BR 4110/1-1, No. KR3831/4-1, and via the TRR 288 (422213477, project A03). We thank Kristin Kliemt and Cornelius Krellner for providing the YbRh₂Si₂ samples, Vladimir Antonov for making the wire bonds to diverse materials, and Marijn Lucas for help with the magnet characterisation. The cell was built, and measurements were conducted at the London Low Temperature Laboratory, and we are grateful to Richard Elsom, Ian Higgs, Paul Bamford, and Harpal Sandhu for excellent technical support.

Open Access This article is licensed under a Creative Commons Attribution 4.0 International License, which permits use, sharing, adaptation, distribution and reproduction in any medium or format, as long as you give appropriate credit to the original author(s) and the source, provide a link to the Creative Commons licence, and indicate if changes were made. The images or other third party material in this article are included in the article's Creative Commons licence, unless indicated otherwise in a credit line to the material. If material is not included in the article's Creative Commons licence and your intended use is not permitted by statutory regulation or exceeds the permitted use, you will need to obtain permission directly from the copyright holder. To view a copy of this licence, visit <http://creativecommons.org/licenses/by/4.0/>.

References

1. F. Pobell, *Matter and Methods at Low Temperatures* (Springer, Berlin, 2007)
2. M. Brando, Development of a relaxation calorimeter for temperatures between 0.05 and 4 K. *Rev. Sci. Instr.* **80**(9), 095112 (2009). <https://doi.org/10.1063/1.3202380>
3. H. Wilhelm, T. Lühmann, T. Rus, F. Steglich, A compensated heat-pulse calorimeter for low temperatures. *Rev. Sci. Instrum.* **75**(8), 2700–2705 (2004). <https://doi.org/10.1063/1.1771486>
4. H. Tsujii, B. Andraka, M. Uchida, H. Tanaka, Y. Takano, Specific heat of the s=1 spin-dimer antiferromagnet Ba₃Mn₂O₈ in high magnetic fields. *Phys. Rev. B* **72**(21), 214434 (2005). <https://doi.org/10.1103/physrevb.72.214434>
5. G.R. Stewart, Measurement of low-temperature specific heat. *Rev. Sci. Instrum.* **54**(1), 1–11 (1983). <https://doi.org/10.1063/1.1137207>
6. O. Bourgeois, S.E. Skipetrov, F. Ong, J. Chaussy, Attojoule calorimetry of mesoscopic superconducting loops. *Phys. Rev. Lett.* **94**(5), 057007 (2005). <https://doi.org/10.1103/physrevlett.94.057007>
7. T. Herrmannsdörfer, S. Rehmann, M. Seibold, F. Pobell, Interplay of nuclear magnetism and superconductivity. *J. Low Temp. Phys.* **110**(1/2), 405–410 (1998). <https://doi.org/10.1023/a:1022565607158>

8. T. Herrmannsdörfer, D. Tayurskii, The impact of nuclear magnetism on superconductivity in a metal with nuclear electric quadrupole splitting: indium. *J. Low Temp. Phys.* **124**(1/2), 257–269 (2001). <https://doi.org/10.1023/a:1017590221423>
9. T. Herrmannsdörfer, P. Smeibidl, B. Schröder-Smeibidl, F. Pobell, Spontaneous nuclear ferromagnetic ordering of in nuclei in AuIn₂. *Phys. Rev. Lett.* **74**(9), 1665–1668 (1995). <https://doi.org/10.1103/physrevlett.74.1665>
10. C. Krellner, S. Taube, T. Westerkamp, Z. Hossain, C. Geibel, Single-crystal growth of YbRh₂Si₂ and YbIr₂Si₂. *Phil. Mag.* **92**(19–21), 2508–2523 (2012). <https://doi.org/10.1080/14786435.2012.669066>
11. K. Kliemt, M. Peters, F. Feldmann, A. Kraiker, D.-M. Tran, S. Rongstock, J. Hellwig, S. Witt, M. Bolte, C. Krellner, Crystal growth of materials with the ThCr₂Si₂ structure type. *Cryst. Res. Technol.* **55**(2), 1900116 (2019). <https://doi.org/10.1002/crat.201900116>
12. J. Knapp, L.V. Levitin, J. Nyéki, A.F. Ho, B. Cowan, J. Saunders, M. Brando, C. Geibel, K. Kliemt, C. Krellner, Electronuclear transition into a spatially modulated magnetic state in YbRh₂Si₂. *Phys. Rev. Lett.* **130**(12), 126802 (2023). <https://doi.org/10.1103/physrevlett.130.126802>
13. L. Levitin, H. van der Vliet, T. Theisen, S. Dimitriadis, M. Lucas, A. Corcoles, J. Nyéki, A. Casey, G. Creeth, I. Farrer, D. Ritchie, J. Nicholls, J. Saunders, Cooling low-dimensional electron systems into the microkelvin regime. *Nat. Commun.* **13**(1), 1–8 (2022). <https://doi.org/10.1038/s41467-022-28222-x>
14. L.V. Levitin et al., Fast current sensing noise thermometry. In preparation (2024)
15. A. Shibahara, O. Hahtela, J. Engert, H. van der Vliet, L.V. Levitin, A. Casey, C.P. Lusher, J. Saunders, D. Drung, T. Schurig, Primary current-sensing noise thermometry in the millikelvin regime. *Philos. Trans. R. Soc. A: Math., Phys. Eng. Sci.* **374**(2064), 20150054 (2016). <https://doi.org/10.1098/rsta.2015.0054>
16. A. Casey, F. Arnold, L.V. Levitin, C.P. Lusher, J. Nyéki, J. Saunders, A. Shibahara, H. van der Vliet, B. Yager, D. Drung, T. Schurig, G. Batey, M.N. Cuthbert, A.J. Matthews, Current sensing noise thermometry: a fast practical solution to low temperature measurement. *J. Low Temp. Phys.* **175**, 764–775 (2014). <https://doi.org/10.1007/s10909-014-1147-z>
17. A. Casey, Current-sensing noise thermometry from 4.2 K to below 1 mK using a DC SQUID preamplifier. *Phys. B: Condens. Matter* (2003). [https://doi.org/10.1016/s0921-4526\(02\)02293-7](https://doi.org/10.1016/s0921-4526(02)02293-7)
18. J. Nyéki, M. Lucas, P. Knappová, L.V. Levitin, A. Casey, J. Saunders, H. van der Vliet, A.J. Matthews, High-performance cryogen-free platform for microkelvin-range refrigeration. *Phys. Rev. Appl.* **18**(4), 041002 (2022). <https://doi.org/10.1103/physrevapplied.18.041002>
19. J.C. Ho, H.R. O'Neal, N.E. Phillips, Low temperature heat capacities of constantan and manganin. *Rev. Sci. Instrum.* **34**(7), 782–783 (1963). <https://doi.org/10.1063/1.1718572>
20. J.C. Ho, N.E. Phillips, Tungsten-platinum alloy for heater wire in calorimetry below 0.1°K. *Rev. Sci. Instr.* **36**(9), 1382–1382 (1965). <https://doi.org/10.1063/1.1719917>
21. J. Butterworth, S. Triqueneaux, Š Midlik, I. Golokolenov, A. Gerardin, T. Gandit, G. Donnier-Valentin, J. Goupy, M.K. Phuthi, D. Schmoranzler et al., Superconducting aluminum heat switch with 3 nΩ equivalent resistance. *Rev. Sci. Instr.* **10**(1063/5), 0079639 (2022). <https://doi.org/10.1063/5.0079639>
22. I. Karakaya, W.T. Thompson, The Ag-Pb (silver-lead) system. *Bull. Alloy Ph. Diagr.* **8**(4), 326–334 (1987). <https://doi.org/10.1007/bf02869268>
23. C.P. Poole, H.A. Farach, R.J. Creswick, R. Prozorov, *Superconductivity* (Elsevier/Academic Press, Amsterdam, 2007), p.650
24. J.B. Johnson, Thermal agitation of electricity in conductors. *Nature* **119**(2984), 50–51 (1927). <https://doi.org/10.1038/119050c0>
25. H. Nyquist, Thermal agitation of electric charge in conductors. *Phys. Rev.* **32**(1), 110–113 (1928). <https://doi.org/10.1103/physrev.32.110>
26. D. Drung, C. Hinrichs, H.-J. Barthelmeß, Low-noise ultra-high-speed dc SQUID readout electronics. *Superconduct. Sci. Technol.* **19**(5), 235–241 (2006). <https://doi.org/10.1088/0953-2048/19/5/s15>
27. D. Drung, C. Assmann, J. Beyer, A. Kirste, M. Peters, F. Ruede, T. Schurig, Highly sensitive and easy-to-use SQUID sensors. *IEEE Trans. Appl. Supercond.* **17**(2), 699–704 (2007). <https://doi.org/10.1109/tasc.2007.897403>
28. A. Kirste, A. Casey, J. Engert, L. Levitin, Comparison of different johnson noise thermometers from millikelvin down to microkelvin temperatures, in: *Proceedings of the 29th International*

- Conference on Low Temperature Physics (LT29), vol 38 (Journal of the Physical Society of Japan, Sapporo, 2023). <https://doi.org/10.7566/jpscp.38.011198>
29. R.L. Rusby, M. Durieux, A.L. Reesink, R.P. Hudson, G. Schuster, M. Kühne, W.E. Fogle, R.J. Soulen, E.D. Adams, The provisional low temperature scale from 0.9 mK to 1 K, PLTS-2000. *J. Low Temp. Phys.* **126**(1/2), 633–642 (2002). <https://doi.org/10.1023/a:1013791823354>
 30. BIPM, SI Brochure—9th Edition, Appendix 2, Mise en Pratique for the Definition of the Kelvin (2019)
 31. 24–Bit, Flexible Resolution PXI Oscilloscope. <http://www.ni.com/en-gb/support/model.pxi-5922.html>
 32. S.N. Tripathi, S.R. Bharadwaj, S.R. Dharwadkar, The Nb–Pt (niobium–platinum) system. *J. Ph. Equilib.* **16**(5), 465–470 (1995). <https://doi.org/10.1007/bf02645357>
 33. H. Okamoto, T.B. Massalski, The Au–Pt (gold–platinum) system. *Bull. Alloy Ph. Diagr.* **6**(1), 46–56 (1985). <https://doi.org/10.1007/bf02871187>
 34. EPO-TEK E4110. <https://www.epotek.com/docs/en/Datasheet/E4110.pdf>
 35. 43 MHz Bandwidth, 16–Bit, Onboard Signal Processing PXI Waveform Generator. <https://www.ni.com/en-gb/support/model.pxi-5441.html>
 36. Keithley 2400. <https://www.tek.com/en/products/keithley/source-measure-units/2400-standard-series-sourcemeater>
 37. E. Schuberth, M. Tippmann, L. Steinke, S. Lausberg, A. Steppke, M. Brando, C. Krellner, C. Geibel, R. Yu, Q. Si, F. Steglich, Emergence of superconductivity in the canonical heavy–electron metal YbRh_2Si_2 . *Science* **351**(6272), 485–488 (2016). <https://doi.org/10.1126/science.aaa9733>
 38. E. Schuberth, S. Wirth, F. Steglich, Nuclear-order-induced quantum criticality and Heavy-Fermion superconductivity at ultra-low temperatures in YbRh_2Si_2 . *Front. Electron. Mater.* (2022). <https://doi.org/10.3389/femat.2022.869495>
 39. A. Steppke, S. Hamann, M. König, A.P. Mackenzie, K. Kliemt, C. Krellner, M. Kopp, M. Lonsky, J. Müller, L.V. Levitin, J. Saunders, M. Brando, Microstructuring YbRh_2Si_2 for resistance and noise measurements down to ultra-low temperatures. *New J. Phys.* **24**(12), 123033 (2022). <https://doi.org/10.1088/1367-2630/aca8c6>
 40. J. Kondo, Internal magnetic field in rare earth metals. *J. Phys. Soc. Jpn.* **16**(9), 1690–1691 (1961). <https://doi.org/10.1143/jpsj.16.1690>
 41. P. Bonville, P. Imbert, G. Jéhanno, F. Gonzalez-Jimenez, F. Hartmann-Boutron, Emission Mössbauer spectroscopy and relaxation measurements in hyperfine levels out of thermal equilibrium: Very–low–temperature experiments on the Kondo alloy Au^{170}Yb . *Phys. Rev. B* **30**(7), 3672–3690 (1984). <https://doi.org/10.1103/physrevb.30.3672>
 42. P. Bonville, J.A. Hodges, P. Imbert, G. Jéhanno, D. Jaccard, J. Sierro, Magnetic ordering and paramagnetic relaxation of Yb^{3+} in YbNi_2Si_2 . *J. Magn. Magn. Mater.* **97**(1–3), 178–186 (1991). [https://doi.org/10.1016/0304-8853\(91\)90178-d](https://doi.org/10.1016/0304-8853(91)90178-d)
 43. I. Nowik, S. Ofer, Mössbauer studies of ^{170}Yb in several paramagnetic salts. *J. Phys. Chem. Solids* **29**(12), 2117–2119 (1968). [https://doi.org/10.1016/0022-3697\(68\)90007-3](https://doi.org/10.1016/0022-3697(68)90007-3)
 44. J. Plessel, M.M. Abd-Elmeguid, J.P. Sanchez, G. Knebel, C. Geibel, O. Trovarelli, F. Steglich, Unusual behavior of the low-moment magnetic ground state of YbRh_2Si_2 under high pressure. *Phys. Rev. B* **67**(18), 180403 (2003). <https://doi.org/10.1103/physrevb.67.180403>
 45. G. Knebel, R. Boursier, E. Hassinger, G. Lapertot, P.G. Niklowitz, A. Pourret, B. Salce, J.P. Sanchez, I. Sheikin, P. Bonville, H. Harima, J. Flouquet, Localization of 4f state in YbRh_2Si_2 under magnetic field and high pressure: Comparison with CeRh_2Si_2 . *J. Phys. Soc. Jpn.* **75**(11), 114709 (2006). <https://doi.org/10.1143/jpsj.75.114709>
 46. J. Flouquet, W.D. Brewer, Hyperfine interaction studies of local moments in metals. *Phys. Scr.* **11**(3–4), 199–207 (1975). <https://doi.org/10.1088/0031-8949/11/3-4/013>
 47. J. Flouquet, Kondo coupling, hyperfine and exchange interactions. *Le J. de Phys. Colloq.* **39**(C6), 6–149361498 (1978). <https://doi.org/10.1051/jphyscol:19786592>
 48. M. Brando, L. Pedrero, T. Westerkamp, C. Krellner, P. Gegenwart, C. Geibel, F. Steglich, Magnetization study of the energy scales in YbRh_2Si_2 under chemical pressure. *Phys. Status Solidi (B)* **250**(3), 485–490 (2013). <https://doi.org/10.1002/pssb.201200771>
 49. L. Steinke, E. Schuberth, S. Lausberg, M. Tippmann, A. Steppke, C. Krellner, C. Geibel, F. Steglich, M. Brando, Ultra–low temperature ac susceptibility of the heavy–fermion superconductor YbRh_2Si_2 . *J. Phys: Conf. Ser.* **807**, 052007 (2017). <https://doi.org/10.1088/1742-6596/807/5/052007>

50. A. Stepke, M. Brando, N. Oeschler, C. Krellner, C. Geibel, F. Steglich, Nuclear contribution to the specific heat of $\text{Yb}(\text{Rh}_{0.93}\text{Co}_{0.07})_2\text{Si}_2$. *Phys. Status Solidi (B)* **247**(3), 737–739 (2010). <https://doi.org/10.1002/pssb.200983062>
51. C. Krellner, S. Hartmann, A. Pikul, N. Oeschler, J.G. Donath, C. Geibel, F. Steglich, J. Wosnitza, Violation of critical universality at the antiferromagnetic phase transition of YbRh_2Si_2 . *Phys. Rev. Lett.* **102**(19), 196402 (2009). <https://doi.org/10.1103/physrevlett.102.196402>
52. F. Giazotto, T.T. Heikkilä, A. Luukanen, A.M. Savin, J.P. Pekola, Opportunities for mesoscopics in thermometry and refrigeration: physics and applications. *Rev. Mod. Phys.* **78**(1), 217–274 (2006). <https://doi.org/10.1103/revmodphys.78.217>

Publisher's Note Springer Nature remains neutral with regard to jurisdictional claims in published maps and institutional affiliations.